

Large Perpendicular Magnetic Anisotropy in Nanometer-Thick Epitaxial Graphene/Co/Heavy Metal Heterostructures for Spin–Orbitronics Devices

María Blanco-Rey,* Paolo Perna,* Adrian Gudin, Jose Manuel Diez, Alberto Anadón, Pablo Olleros-Rodríguez, Leticia de Melo Costa, Manuel Valvidares, Pierluigi Gargiani, Alejandra Guedeja-Marron, Mariona Cabero, María Varela, Carlos García-Fernández, Mikhail M. Otrokov, Julio Camarero, Rodolfo Miranda, Andrés Arnau, and Jorge I. Cerdá



Cite This: *ACS Appl. Nano Mater.* 2021, 4, 4398–4408



Read Online

ACCESS |



Metrics & More



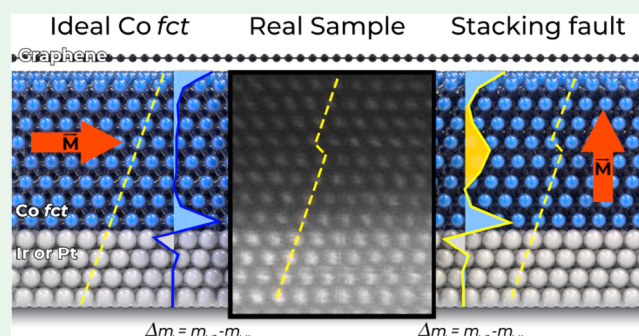
Article Recommendations



Supporting Information

ABSTRACT: Nanometer-thick epitaxial Co films intercalated between graphene (Gr) and a heavy metal (HM) substrate are promising systems for the development of spin–orbitronic devices due to their large perpendicular magnetic anisotropy (PMA). A combination of theoretical modeling and experiments reveals the origin of the PMA and explains its behavior as a function of the Co thickness. High quality epitaxial Gr/Co_n/HM(111) (HM = Pt, Ir) heterostructures are grown by intercalation below graphene, which acts as a surfactant that kinetically stabilizes the pseudomorphic growth of highly perfect Co face-centered tetragonal (*fcc*) films, with a reduced number of stacking faults as the only structural defect observable by high-resolution scanning transmission electron microscopy (STEM). Magneto-optic Kerr effect (MOKE) measurements show that such heterostructures present PMA up to large Co critical thicknesses of about 4 nm (20 ML) and 2 nm (10 ML) for Pt and Ir substrates, respectively. X-ray magnetic circular dichroism (XMCD) measurements show an inverse power law of the anisotropy of the orbital moment with Co thickness, reflecting its interfacial nature, that changes sign at about the same critical values. First principles calculations show that, regardless of the presence of graphene, ideal Co *fcc* films on HM buffers do not sustain PMAs beyond around 6 mLS due to the in-plane contribution of the inner bulk-like Co layers. The large experimental critical thicknesses sustaining PMA can only be retrieved by the inclusion of structural defects that promote a local *hcp* stacking such as twin boundaries or stacking faults. Remarkably, a layer resolved analysis of the orbital momentum anisotropy reproduces its interfacial nature, and reveals that the Gr/Co interface contribution is comparable to that of the Co/Pt(Ir).

KEYWORDS: magnetic multilayers, perpendicular magnetic anisotropy, spin–orbit coupling, MOKE, XMCD, DFT



1. INTRODUCTION

Heterostructures with large perpendicular magnetic anisotropy (PMA)^{1–10} are a key ingredient in the emerging field of spin orbitronics,¹¹ aimed at the development of functional, high-speed, low-energy consumption nanodevices.¹² Maximizing the PMA is essential to downscale the size of data storage spintronic devices such as spin transfer torque magnetic random access memories (STT-MRAM).¹² In metallic multilayer heterostructures, the effective PMA is determined by the morphology plus an intricate interplay of structural and electronic effects, the latter being essentially dependent on the crystal field and the spin–orbit interaction (SOI) strength.¹ This is often enhanced by growing alternate ultrathin layers of magnetic (e.g., Co or Fe) films and heavy metals (HM), like Pt or Ir, which induce strong SOI at the interfaces by a proximity effect.^{2,13–15} However, as the

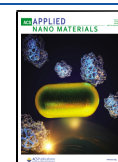
thickness of the constituent layers increases, the PMA is severely reduced, since the morphology and the structure of the magnetic films may degrade, the weight of the interfaces is reduced and the low-dimensional behavior is lost.

Design, fabrication, and characterization of multilayer structures with large PMA is a thriving open research area. The growth conditions determine the resulting morphology, that is, two-dimensional vs three-dimensional films, structural

Received: December 16, 2020

Accepted: February 24, 2021

Published: March 16, 2021



details,⁴ such as the crystalline perfection and the stacking sequence of atomic planes in each constituent layer. The latter may include dislocations, stacking faults (SFs)^{16–18} or twin boundaries (TBs), as well as strain or compositional disorder due to intermixing. Among all of them, a three-dimensional morphology rapidly cancels interfacial effects in thin ferromagnetic films. Recently, a new technique^{19,20} has been developed to grow high quality Co(111)/Pt(111) heterostructures by intercalation of Co atoms in Gr/Pt(111) systems (see Figure 1(A)), with graphene playing the role of a surfactant, a similar behavior as in intercalation on a Ir(111) buffer.^{21–24} The result is an atomically flat film of highly perfect, pseudomorphic Co in a face centered tetragonal (*fcc*) crystalline structure, laterally expanded to adjust to the lattice parameter of Pt, which keeps a giant PMA for unusually large thickness of the nanometer-thick Co film.¹⁹

In this work, we unravel the origin of this large PMAs in epitaxial *fcc* Co films intercalated between graphene and HM substrates, that is, Gr/Co_{*n*}/HM(111) (HM = Pt, Ir, and *n* being the number of Co layers). Magneto-optic Kerr effect (MOKE) measurements reveal that these heterostructures develop PMA up to unusually large Co thicknesses of about 4 nm (≈ 20 MLs) and 2 nm (≈ 10 MLs) for Pt and Ir substrates, respectively. Consistently, X-ray magnetic circular dichroism (XMCD) experiments evidence that at the same critical thicknesses the orbital momentum anisotropy is switched from out-of-plane to in-plane. Detailed state-of-the-art *ab initio* calculations within density functional theory (DFT) allow breaking down the contributions responsible for this behavior, the most important of them coming from local hexagonal closed packed (*hcp*) stackings in the Co film induced by TBs or SFs. These calculations are converged with unprecedented accuracy for a number of structural scenarios (Co film thicknesses in the 1–20 MLs range, different Gr moiré patterns, inclusion of TBs/SFs in the Co film, and intermixing at the interfaces). Our high-resolution scanning transmission electron microscopy (STEM) measurements indeed confirm the presence of SFs in both Pt- and Ir-based systems that inevitably appear associated with atomic steps at the Co/HM interface. Extensive theoretical modeling of various TBs in the face-centered cubic (*fcc*) stacked intercalated Co films shows that these defects play a fundamental role in sustaining the PMA up to the observed large Co thicknesses. Finally, we find a sizable orbital momentum anisotropy induced by graphene in the two outer Co atomic planes, which, in spite of the much weaker SOI in graphene, appears to be comparable to that at the Co/Pt(Ir) interface.

2. RESULTS AND DISCUSSION

The structural characterization of the epitaxial Gr/Co/HM(111) (HM = Pt, Ir) heterostructures is shown in Figure 1. The intercalated Co films are atomically flat as revealed by STM.²⁰ The LEED patterns observed after intercalation (Figure 1(A)) are identical to the ones seen for pristine Gr/Pt(111) and Gr/Ir(111) corresponding to the moiré patterns also visualized for both substrates with STM^{22,25,26} and different from the (1 × 1) pattern observed for Gr/Co(0001). This confirms that (i) graphene is floating on top of the Co films, that is, Co is intercalated between the HM(111) buffer layer and graphene; and (ii) the Co films are pseudomorphic with the Pt and Ir substrates, that is, laterally expanded to adjust to the lattice parameter of the substrate. The presence of Co underneath graphene is verified by XPS, as

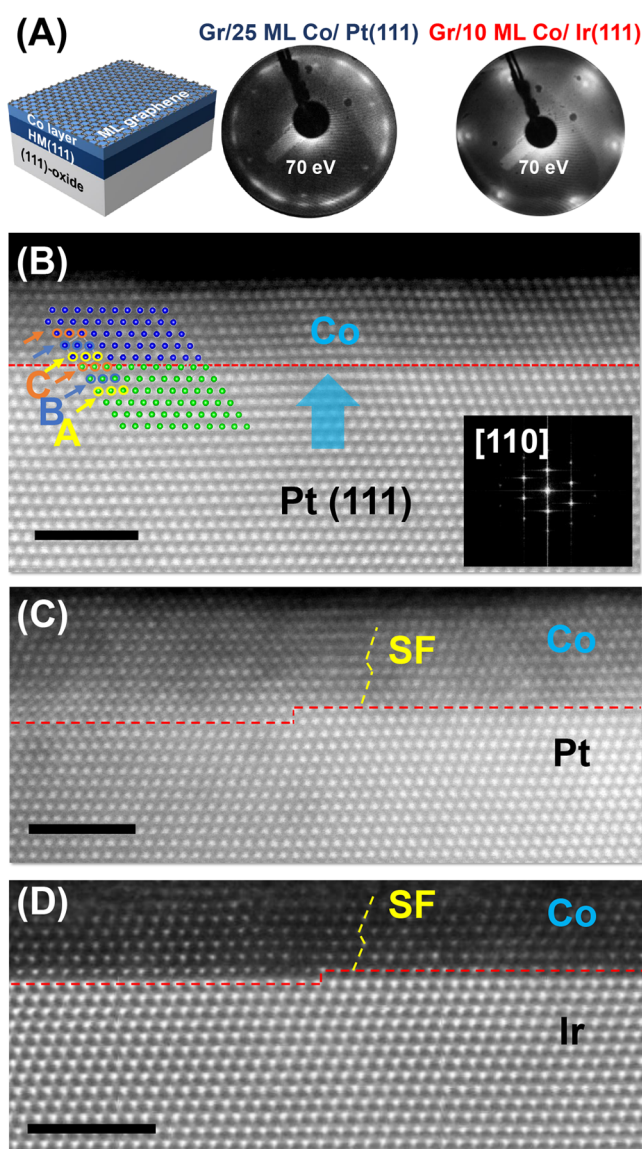


Figure 1. Structural and microscopic characterization of epitaxial Gr/Co_{*n*}/HM heterostructures. (A) Perspective sketch of the samples grown on an oxide buffer and representative LEED patterns acquired at 70 eV on the indicated samples after Co deposition and intercalation. The moiré superstructures of Gr on Pt(111) and Ir(111) are preserved after Co intercalation. (B), (C), and (D) High angle annular dark field (HAADF) high resolution STEM images of the interfaces upon intercalation of 10 LL of Co on Gr/Pt(111) and Gr/Ir(111). Panel (B) corresponds to Co on Gr/Pt(111). The inset shows the fast Fourier transform of the STEM image, acquired along the [110] projection, revealing the high crystalline coherence between Co and HM layers. The sketch overlaid across the HM/Co interface highlights the ABCABC atomic plane stacking sequence of the *fcc* lattice, marked with colored arrows, and the pseudomorphic arrangement of the Co film. Panels (C) and (D) show high magnification images of stacking faults in 10 MLs thick Co over Pt(111) (C) and Ir(111) (D) buffers grown epitaxially onto SrTiO₃ (STO) (111) substrates. Stacking faults can be observed in both samples, marked with yellow dashed lines. The approximate interface positions are marked with red dashed lines. Occasional atomic steps are visible. The scale bars represent 2 nm.

demonstrated elsewhere.²⁰ The high angle annular dark field (HAADF) STEM images, shown in Figure 1(B–D) and Supporting Information (SI) Figures S1 and S2, reveal the

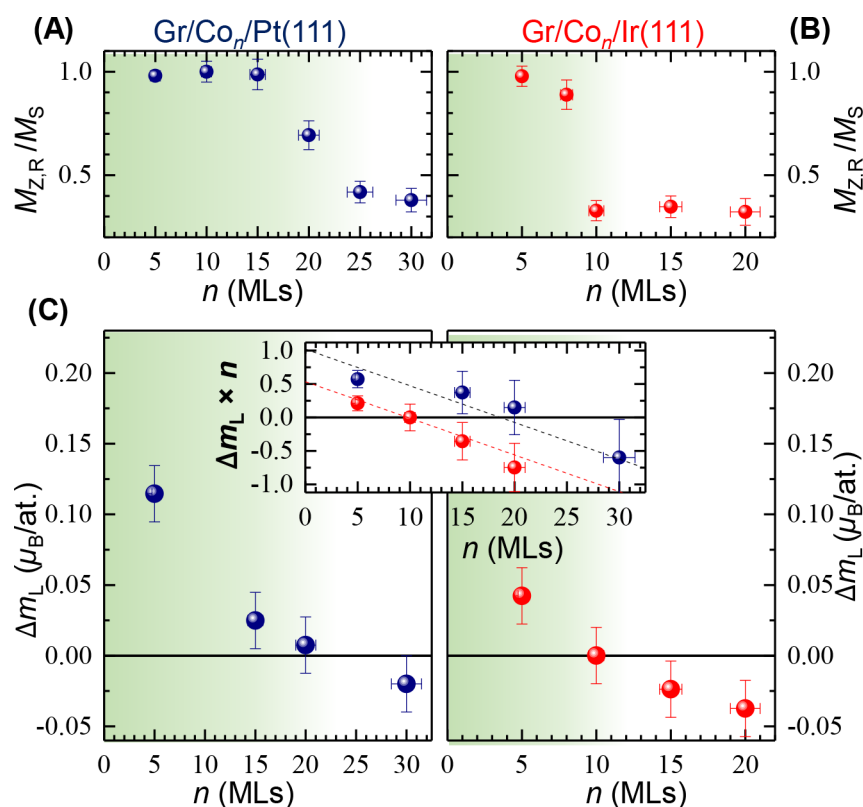


Figure 2. Quantified magnetic parameters of epitaxial Gr/Co/HM heterostructures. Room-temperature thickness-dependent remanence, of (A) Gr/Co/Pt(111) and (B) Gr/Co/Ir(111) samples, and (C) anisotropy of orbital moment. $M_{z,R}/M_S$ is the remanent perpendicular magnetization normalized to the saturation magnetization. Symbols are the data derived from polar-MOKE and XMCD measurements, such as the ones shown in Supporting Information SI Figures S3 and S4, respectively. (C) The anisotropy of the orbital moment (Δm_L) is computed from the difference of orbital moments derived from sum-rule analysis at normal (NI) and grazing (GI) incidence geometries ($\Delta m_L = m_{L,NI} - m_{L,GI}$), assuming a number of Co-*d* holes of 2.49. The shadowed areas in the graphs highlight the corresponding PMA critical Co thickness, that is $n_C = 20$ ML and $n_C = 10$ ML for Pt and Ir buffers, respectively. Notice the coincidence of n_C and the change of sign of Δm_L . The inset displays the corresponding anisotropy of orbital moment times Co thickness versus Co thickness. Notice the similar linear slope (bulk contribution) and different vertical axis intercept (interface contribution), twice as large in the case of Gr/Co_n/Pt.

predominant *fcc* stacking of the Co layers intercalated and the pseudomorphic arrangement of the Co film, as well as the presence of stacking faults (SFs) at the Co layer near the Pt (Ir) steps underneath. The lateral (tensile) strain induced by the HM substrate results in a tetragonal distortion²⁷ of the *fcc* Co toward a *fct* structure.

A well-defined perpendicular magnetic anisotropy (PMA), that is, out-of-plane magnetization easy axis, in Gr/Co_n/HM heterostructures has been identified at 300 K below a critical Co thickness (n_C) by polar magneto-optic Kerr effect (polar-MOKE) and X-ray magnetic circular dichroism (XMCD) measurements. From the polar-MOKE hysteresis loops with the external field applied to the surface normal, the remanence and saturation magnetizations, $M_{z,R}$ and M_S , respectively, are determined as a function of Co thickness (n) for samples grown on Pt and Ir (see SI Figure S3). The corresponding ratios $M_{z,R}/M_S$ are shown in Figure 2. In the case of the Pt(111) substrate, the hysteresis loops evolve smoothly from a square-shaped loop with large coercive field, that is, 100 mT for $n = 5$ Co MLs to an S-shaped loop with reduced remanence values above n_C . Figure 2(A) suggests that the magnetization switches from out-of-plane to in-plane upon growth of between $n = 15$ –25 Co atomic planes, that is, $n_C \sim 20$ ML. The hysteresis behavior change is more abrupt in the case of Ir(111), where the magnetization reorientation happens at a

lower Co thickness value around $n_C \sim 10$ ML as can be seen in Figure 2(B).

Angular dependence XMCD measurements performed at room temperature (RT) in Gr/Co_n/HM heterostructures confirm qualitatively the aforementioned polar-MOKE observations. The comparison between the dichroism spectra acquired in normal incidence (NI) and grazing incidence (GI) geometries for the different Co thicknesses directly shows: (i) PMA for $n < n_C$ (i.e., larger NI dichroism signal, as Figure S3 shows), (ii) preferential in-plane orientation for $n > n_C$ (i.e., larger GI dichroism signal, as depicted the bottom graphs of Figure S4), (iii) the critical thickness is higher in the case of the Pt buffer, that is, for HM = Pt, and (iv) the quantitative analysis of the XMCD spectra provides the microscopic interfacial picture on the origin of the PMA. Sum rules applied to the XMCD spectra^{28,29} recorded at 6 T external magnetic field (see SI Figure S4) provide the projection of the orbital magnetic moments along the applied field (same as incident light) direction. Following the standard application of the sum rules,³⁰ Figure 2(C) shows the orbital moment difference Δm_L between out-of-plane and in-plane incidence ($\Delta m_L = m_{L,NI} - m_{L,GI}$), normalized by the number of holes $n_h = 2.49$ in the Co-3*d* band extracted from the XMCD spectra. There is a sign change in this quantity between $n = 20$ and $n = 30$ MLs of Co for Co/Pt and around $n = 10$ MLs for Co/Ir. These thicknesses derived from the XMCD sum rule analysis are

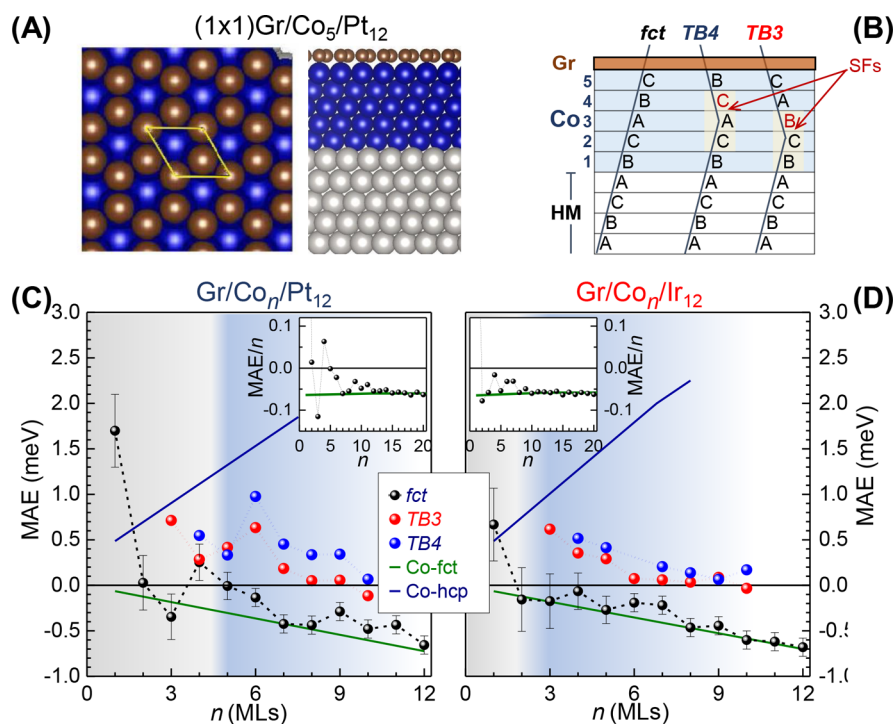


Figure 3. Calculated magnetocrystalline anisotropy energy (MAE) for (1×1) -Gr/Co_n/HM₁₂ heterostructures. (A) Representative top and side views of the model used for the ideal *fct* structure with HM = Pt and $n = 5$ MLs. (B) Scheme of the different layer sequences used, without stacking faults (ideal *fct*) and with one twin boundary starting at the third (TB3) or fourth (TB4) layer of the Co film. (C) and (D) MAE as a function of the Co thickness n calculated for the stacking sequences indicated in panel B, in the case of HM = Pt and Ir, respectively. Symbols correspond to (1×1) -Gr/Co_n/HM₁₂ heterostructures with different stacking sequences (black, red, and blue are used for ideal *fct*, TB3 and TB4, respectively), whereas continuous lines refer to bulk Co phases (*fcc* and strained *hcp* indicated in dark blue and green, respectively). Shaded areas emphasize the predicted PMA Co critical thickness, n_c , for ideal *fct* films. Insets show the MAEs normalized by the Co thickness, n , for the ideal *fct* films with n up to 20 MLs, in order to illustrate their convergence toward the bulk Co-*fcc* values indicated by the horizontal green line.

similar to those that produce a significant drop in the $M_{Z,R}$ value in MOKE. This is a proof of consistency between both techniques, which is further supported by DFT calculations of the magnetization, as it will be shown later. The large PMA and Co critical thickness are reproduced by comparing MOKE and XMCD data taken at various sample locations at different samples. The XMCD analysis also shows that there is not significant anisotropy in the spin magnetic moments (see SI Figure S6).

According to Bruno,^{31,32} Δm_L can be written as the combination of bulk and interfaces contributions, that is, $\Delta m_L = \Delta m_L(\text{Co}_{\text{bulk}}) + [\Delta m_L(\text{Gr/Co}) + \Delta m_L(\text{Co/Pt})]/n$. This expression should hold as long as the interfaces are flat and the Co film is thick enough for the internal Co layers to be considered as an effective bulk-like contribution. The latter includes the defect-free *fct* contribution and further interfacial contributions, such as stacking defects, as those observed in Figure 1(C,D). Experimentally, when Δm_L is multiplied by n (see inset of Figure 2(C)), we observe a linear dependence with the Co thickness with similar slope for both Pt and Ir buffer cases, which may be assigned to the effective bulk Co contribution. The different vertical axis intercepts correspond instead to the interfacial contributions, twice as large for Gr/Co/Pt(111) than for Gr/Co/Ir(111). A similar effective bulk contribution suggests a similar fraction of defect-free *fct* and stacking faults in the Gr/Co_n/HM heterostructures grown on a similar STO substrate, for both Pt and Ir cases, which could be associated with the substrate having on average the same number of steps. A priori, the experimental data are not

sufficient to determine the contribution of each interface from the vertical axis intercept. Considering a negligible Gr/Co interfacial contribution for both Pt and Ir cases, the experimental intercepts can be explained with an interfacial Co/HM contribution two times larger for the Pt case. In contrast, there is the observation of the unprecedented very high critical thickness that cannot be understood without the presence of the Gr/Co interface.

In the following, we rationalize the experimental findings by presenting DFT-derived magnetic anisotropy energies (MAEs) and orbital magnetic moments (OMMs) for ideal and defected Gr/Co_n/HM heterostructures (see Figure 3(A),(B)) after including the SOI self-consistently.

Ideal *fct* Co Films. Figure 3(C),(D) show the calculated MAEs for (1×1) -Gr/Co_n/HM₁₂ slabs (black dots and lines) as a function of the Co thickness, n , assuming an ideal *fcc* stacking throughout the film (see SI Section 4 for details on the relaxed geometries). Inspection of the curves reveals two different regimes with similar behaviors in both systems (notice that positive values of the MAE correspond to PMA). At small Co thicknesses, $n < 9$ in Pt and $n < 7$ in Ir supported films, the anisotropies are highly nonlinear presenting multiple oscillations. Large PMA values are only attained in the ultrathin limit $n = 1$, while small or negligible PMAs also appear at slightly larger thicknesses ($n = 2, 4-5$ for Pt and $n = 4$ for Ir). In the second region, $n \geq 9$ (7) for Pt (Ir), in-plane magnetization has clearly set in and the MAEs present a quasi-linear behavior with the Co film thickness. The absence of strong oscillations in this region indicates that the individual

Table 1. Difference in the Calculated MAE (in meV) between a (1×1) -Gr/Co_n/HM₁₂ Slab with a TB Located at Layer $i = 2-9$ from the Co/HM Interface (Fig. 3(B)) and That of the Same Slab without Defects (Ideal Co-*fcc*)

i	1	2	3	4	5	6	7	8	9
Pt	0.11	0.37	0.55	0.62	0.68	0.66	0.69	0.47	0.75
Ir	0.81	0.57	0.77	0.42	0.49	0.53	0.62	0.35	0.74

contributions from the Co/Gr and HM/Co interfaces are essentially decoupled. The slopes may be associated with the MAE of a tetragonally distorted Co *fcc* single crystal with the in-plane lattice parameter fixed to that of the HM (green lines). This is best seen in the insets, where the MAEs normalized by the number of Co layers, up to $n = 20$, are shown along with that of the corresponding Co bulk *fcc*, which is weakly in-plane anisotropic. Furthermore, the coincidence between the two lines, within less than 0.01 meV for $n \geq 12$ (10) in the case of Pt (Ir), reveals that, once the film is thick enough and finite quantum size effects are removed, the net contribution of the two interfaces in both systems is negligible.

Overall, the calculated MAEs are in qualitative agreement with MOKE and XMCD data, in the sense that they reproduce the switch from out-of-plane to in-plane as the Co film grows, with the transition occurring earlier in Ir than in Pt. However, the calculated critical thicknesses for the MAE switch, n_C , are notably smaller than the observed values. Let us recall that in the simulations, apart from ultrafine k -meshes larger than 70×70 , we have employed a 12 layer thick HM buffer layer (see SI Section 8), which is much larger than those typically used in similar theoretical studies.^{18,33–37} In order to ensure converged MAE values below 0.1 meV, we have also avoided the use of perturbative approaches (see SI Section 7). Still, further sources of inaccuracy could be ascribed to Co-HM intermixing at the interface, or to the particular moiré pattern between the Gr and Co unit cells or to the shape anisotropy (SA), which has been neglected so far.

Indeed, some degree of compositional disorder may well be present close to the Co/HM interface,²⁰ as can be inferred from the variable intensity at some interface atomic planes in the high-resolution STEM images in Figure 1 and SI Figures S1 and S2. As shown in SI Section 5, Pt–Co mixing at the early stages of the Co growth is a stabilizing factor toward the *fcc* structure of the films versus the energetically favored *hcp* stacking. Still, interfacial mixing should have a minor effect in the MAEs of thick films once the bulk regime has been reached.

The magnetocrystalline anisotropy is extremely sensitive to the interfacial electronic structure. For example, it can be tuned by oxidation, as this process involves charge transfer.^{14,38} Although hybridization and charge transfer at the Gr/Co interface are reduced, compared to Co/metal–oxide interfaces, they are by no means negligible. Furthermore, they depend on fine structure details. The influence of the precise Gr/Co interface geometry on the MAE has been addressed by performing analogous calculations for (1×1) -Co_n/HM₁₂ slabs, that is, without the Gr capping layer on top, as well as for Gr/Co_n/Pt₅ slabs assuming two standard Pt/Gr moiré patterns. Results for these scenarios are presented in SI Section 6. It turns out that large deviations in the MAEs of up to 0.5 meV or even larger are always constrained to the ultrathin limit ($n \leq 4$), in analogy with the case of unstrained Co multilayers with *hcp* stacking.³⁴ As n increases, the relative contribution of the vacuum/Co or Gr/Co interfaces is reduced and the MAE of the films also approaches the bulk Co *fcc* limit. We have

accounted for the uncertainty on the MAEs due to the precise moiré pattern in Figure 3 via large error bars that decrease with the Co thickness as interface contributions become less relevant. However, even after considering such ample errors, the theoretical critical thicknesses hardly change and remain considerably smaller than the experimental ones.

Concerning the shape anisotropy, as shown in SI Section 9, the SA of ideal (monodomain) *fcc* Gr/Co_n/HM films favors in-plane magnetization, that is, negative MAE values, with an energy contribution that evolves almost linearly with n and, therefore, its incidence on the total MAEs would be to even further reduce the PMA value. Nevertheless, we have excluded the SA term in Figure 3 since, in real samples, the existence of multiple domains with different/opposite magnetization directions during magnetization reversal³⁹ should reduce considerably its contribution.

Stacking Defects in the *fcc* Films. The above analysis demonstrates that perfect *fcc* Co films cannot hold PMAs at large Co thicknesses. However, from the STEM images shown in Figure 1 and SI Figure S1 and S2, structural defects in the grown samples are common, mainly in the form of SFs or TBs. The appearance of a TB (SF) requires the *hcp* stacking of one (two) Co layers, –ABC–A/B/A–ABC– (–ABC–A/B/A/B–CAB–) and, therefore, incorporates an additional interface into the film which could well delay reaching the bulk *fcc* limit. Indeed, this type of defect is known to significantly alter the band structure of the Co film¹⁷ (details on the electronic band structure of Gr/Co₁₀/HM₁₂ films and the derived interfacial contributions to the MAE can be found in SI Figures S14–S17). We have addressed this possibility by inserting a single TB in the Gr/Co_n/HM₁₂ films. In Figure 3(C,D) we have included the resulting MAEs when the TB (that is, the *hcp* stacked layer) is incorporated at the third (red dots and lines) or fourth (blue) Co atomic plane starting from the Co/HM interface (see panel B in the same figure). Remarkably, in both cases the appearance of the TB yields a large shift of around 1 meV in the MAE toward PMA when compared to the defect-free case (black dots). After this initial large jump, the film again approaches the bulk *fcc* limit but this time with an additional and rather large interfacial contribution associated with the TB, which shifts the critical thicknesses of the films up to the 10 ML range, in better agreement with the experiments.

Table 1 summarizes the interfacial contributions to the MAE for a TB appearing in any of the Co layers in a (1×1) -Gr/Co₁₀/HM₁₂ slab. They always attain positive values, well above 0.6 meV in many cases, although no clear trend with the TB location can be envisaged due to interference effects between the three interfaces. In the case of Ir, where the experimental switch of the MAE occurs at around $n_C = 10$ MLs, a single TB (on average) across the *fcc* Co film would be sufficient to overcome the in-plane bulk-like contribution of the ideal *fcc* film (see dark line Figure 3(D)). In the case of Pt, where the critical thickness is as large as $n_C = 20$ MLs, the required out-of-plane TB contribution would be of the order of 1.3 meV, corresponding to around two TBs on average throughout the film. Therefore, stacking defects in the Co *fcc* films represent a

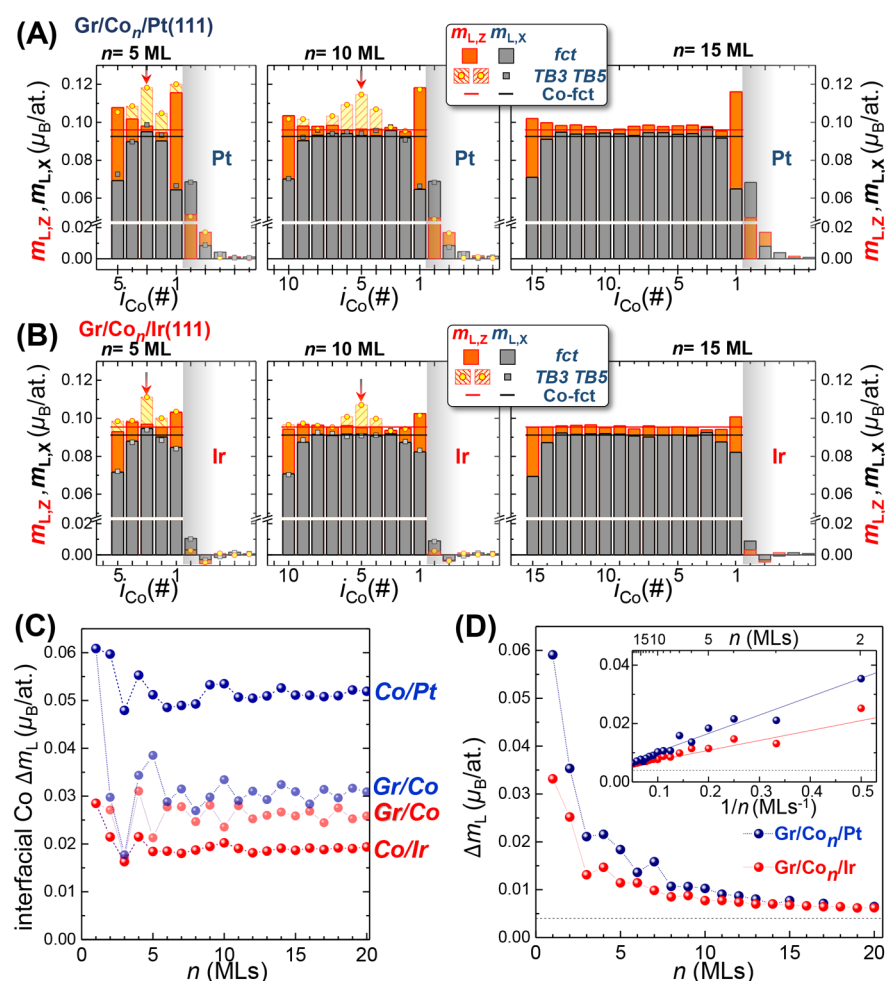


Figure 4. Calculated layer-resolved orbital moments in Gr/Co/HM heterostructures for (A) (1×1) -Gr/Co_n/Pt₁₂ and (B) (1×1) -Gr/Co_n/Ir₁₂ slabs and for indicated n . Red (black) bars correspond to out-of-plane $m_{L,z}$ (in plane $m_{L,x}$) projections of a defect-free slab with a Co *fct* sequence. Bars with circle (square) symbols indicate the corresponding values when a TB defect is introduced at the third ($i_{Co} = 3$) and fifth ($i_{Co} = 5$) Co planes for the $n = 5$ and 10 slabs, respectively. Solid lines refer to the bulk values. (C) Orbital magnetic moment anisotropy ($\Delta m_L = m_{L,z} - m_{L,x}$) of the interfacial Co atoms as a function of the Co slab thickness n , for Pt (blue) and Ir (red) buffer layers. The light and dark lines refer to the Gr/Co and Co/HM interfaces, respectively. (D) Effective orbital magnetic moment anisotropy (Δm_L^{eff}) as a function of the Co thickness for the indicated heterostructures. The dotted lines indicate the averaged value of the inner Co layers. The inset shows that Δm_L^{eff} follows an inverse law with n , that is, interfacial nature, whereas the slope is twice in the case of Gr/Co/Pt.

robust and necessary ingredient to achieve PMAs at large thicknesses. Such a large interfacial contribution may be understood from the fact that a strained Co *hcp* crystal presents large PMAs of 0.49 and 0.56 meV/atom at the Pt and Ir in-plane lattice constants, respectively (dark blue lines in Figure 3(C,D)), and the presence of a TB can be considered as an initial stage toward an *hcp* stacking. Furthermore, since SFs comprise two consecutive locally stacked *hcp* layers, their PMA contribution is expected to be larger than that of a single TB. As a representative example, a SF placed at the second and third Co layers in a Gr/Co₄/Pt₁₂ film yields a PMA more than twice as large than if only a single TB is considered (1.27 meV versus 0.55 meV, respectively).

Orbital Magnetic Moments. We next turn our attention to the orbital magnetic moments (OMMs) in the Co films. Figure 4(A),(B) show the OMMs projected on individual Co and first interfacial HM atoms for a Pt₁₂ and Ir₁₂ buffer layer, respectively, calculated along the out-of-plane, $m_{L,z}$, and in-plane, $m_{L,x}$, spin quantization axes. We include the layer resolved OMMs for two thin $n = 3, 5$ and a thick, $n = 10$, Co

films (equivalent data for other thicknesses are presented in SI Figure S9). If we first focus on the ideal *fct* films and the thick $n = 10$ limit, both $m_{L,x}$ and $m_{L,z}$ remain fairly constant across the Co layer, with clear deviations only at the upper and lower interfaces. The m_L values at the inner layers of the slabs approach those of their respective bulk *fct* phases (SI Table S4), confirming that the bulk limit has been reached at these thicknesses. At the interfaces, the Co OMMs behave differently depending on the spin quantization axis; while $m_{L,x}$ is strongly reduced at both sides of the Co layer, $m_{L,z}$ shows an increase in most of the cases. Hence, the calculated orbital magnetic moment anisotropy (OMMA), defined as $\Delta m_L = m_{L,z} - m_{L,x}$, remains positive across the entire Co film with a marginal value of $\sim 0.004 \mu_B$ at the inner layers, but presenting an enhancement of 1 order of magnitude at the interfaces. When one considers the thinner slabs ($n = 3, 5$), similar conclusions can be drawn for both interfaces and both HMs, except that now the film is not thick enough to develop a plateau at the central layers.

In panel C we present the evolution of the OMMA projected on the first (Co_{Gr}) and last ($\text{Co}_{\text{Pt,Ir}}$) Co layers as a function of the film thickness. At the Gr/Co side, and apart from strong oscillations in the $n \leq 5$ range specially for Pt (light blue line), Δm_{L} remains fairly constant around $0.03 \mu_{\text{B}}$ and slightly smaller for Ir (light red line). It is interesting to note that, despite the OMMs projected on the C atoms are negligible, such large OMMA is induced by the Gr layer. As shown in SI Figure S9, when the Gr capping layer is removed the projections of $m_{\text{L,X}}$ and $m_{\text{L,Z}}$ at the first Co layer both show a similar enhancement of up to $\sim 0.13 \mu_{\text{B}}$, but their difference Δm_{L} becomes negligible. Hence, the Gr layer introduces a highly localized OMM anisotropy at the top of the Co film, otherwise absent, by strongly reducing $m_{\text{L,X}}$ compared to a smaller decrease of $m_{\text{L,Z}}$, the effect being independent of the nature of the HM buffer layer. On the other hand, at the lower Co/HM interface there exist clear differences between the two HMs (dark blue and red lines in Figure 4(C)). For Co_{Ir} we find an interfacial OMMA of $\sim 0.02 \mu_{\text{B}}$, whereas at the Co_{Pt} layer, it is considerably larger ($\sim 0.05 \mu_{\text{B}}$). We also note that the OMMs in the Ir buffer drop to very small values, even marginally negative, already at the second layer, whereas the decay is less pronounced in the Pt buffer and the OMMs remain positive. In accordance with Hund's rules, the induced spin moments at the interface HM atoms follow the same trend. They are larger at the Pt layer ($0.19 \mu_{\text{B}}$ at the first interface atomic plane and $0.08 \mu_{\text{B}}$ at the second, in good agreement with experimental values observed in Co/Pt interfaces⁴⁰) than in Ir (0.11 and $-0.05 \mu_{\text{B}}$), where the decay is faster also presenting an inversion of sign (antiferromagnetic coupling) at the second layer. Therefore, the orbital moment in the HM buffer layer may be interpreted as a proximity effect, which is stronger in Pt(111) as compared to Ir(111). In the same line, we recall that Belabbes et al.⁴¹ also found clear differences in the Dzyaloshinskii–Moriya interaction strength between the Co/Pt(111) and Co/Ir(111) systems.

Last, we address the OMMs associated with a TB. The red circles in Figure 4(A),(B) correspond to the OMMs for defected Co films. In the $n = 5$ case the TB has been incorporated at the third ($i_{\text{Co}} = 3$) Co layer, while in the thicker $n = 10$ slab at the fifth ($i_{\text{Co}} = 5$) layer. Notably, in all cases, $m_{\text{L,Z}}$ shows a pronounced peak precisely at the location of the *hcp* stacked layer, whereas $m_{\text{L,X}}$ remains essentially unchanged. Since the same behavior is reproduced for all other locations of the TB in the Co film (not shown), we conclude that an *hcp* stacked layer consistently yields a localized increase of the OMMA.

In order to compare the theoretical OMMA against the X-ray absorption data shown in Figure 2(B), we define an effective OMMA for the Co atoms in each slab as $\Delta m_{\text{L}}^{\text{eff}} = \frac{1}{n} \sum_{i=1}^n (m_{\text{L,Z}}^i - m_{\text{L,X}}^i)$, where the index i runs over the Co atomic planes. Figure 4(D) shows the resulting values in the defect-free case as a function of thickness for both HM buffer layers. The two curves show a rapid decrease with the Co thickness governed by the $1/n$ factor. Indeed, the $\Delta m_{\text{L}}^{\text{eff}}$ data points can be linearly fitted (see inset), with slopes following the experimental trend shown in the inset of Figure 2, namely around twice larger in the case of the Pt buffer. For each thickness, the main contributions to the effective OMMA are those of the Co_{Gr} and Co_{HM} interface atoms (highlighted in Figure 4(D)) as well as those displaying a local *hcp* stacking in the defected slabs. Overall, the theoretical effective OMMA

curves are in reasonable qualitative agreement with the XMCD data (see Figure 4(D) and Figure 2(C)). Still, there are relevant differences which deserve a further discussion.

First, the calculated OMM values are significantly underestimated by a factor of around three with respect to the experimental ones. Even after the inclusion of TBs close to the surface, which lead to an overall increase of the $\Delta m_{\text{L}}^{\text{eff}}$ values (not shown), a significant experiment-theory difference remains. We ascribe it to the inherent limitation of DFT in the treatment of the electronic correlations,⁴² which is well-known to underestimate (overquench) OMMs of isolated magnetic atoms on surfaces,^{43,44} and has also been noted, for instance, in ultrathin magnetic films.⁴⁵

Second, the XCMD results point to a change of sign in Δm_{L} at similar critical thicknesses at which the MAE also switches. At contrast, the calculated OMMA remains always positive at every Co plane and for all thicknesses considered, regardless if the MAE is out-of- or in-plane.¹ We recall that a direct relationship between the MAE and the OMMA, as the experiments here suggest, is far from having a trivial explanation.^{32,45–49} As a matter of fact, despite the strong SOI conferred by Pt and Ir to the band structure, the correlation between the two properties is not guaranteed, as shown, for instance, in $3d - 5d$ magnetic alloys⁴⁸ and thin-film heterostructures.^{45,49}

From a theoretical point of view, the OMMA and the MAE are expected to be proportional only under the following conditions:⁵⁰ the SOI strength must be small enough for the MAE to be treated as a second-order perturbation effect on the electronic wave functions, the anisotropic part of the spin distribution (quadrupole contribution) must be negligible and the orbital ground state must be non degenerate. The strained Co *fcc* bulk limit already represents an example where any of the above conditions is not fulfilled, as the DFT-derived in-plane MAE is associated with an out-of-plane OMMA (see SI Section 10 for a more detailed discussion). Finally, it is also timely to recall that the typical formulation of the sum rules for XMCD data^{28,29,51} is based on an atomic orbital picture instead of an orbital magnetization. Therefore, it does not account for the effect of the itinerant electron many body wave function, but it gives an effective orbital moment that has a great practical importance for interpreting XMCD spectra.^{52–54}

3. SUMMARY AND CONCLUSIONS

The magnetic anisotropy of Gr/ Co_n /HM(111) (Gr = graphene, HM = Pt,Ir) heterostructures, grown by thermally activated Co intercalation, has been characterized experimentally by MOKE and XMCD with focus on the evolution of the magnetic properties with Co thickness. This growth technique produces a pseudomorphic film with ABC stacking (*fcc* structure), which shows perpendicular magnetic anisotropy (PMA) up to 20 and 10 MLs on Pt and Ir substrates, respectively, as revealed by MOKE measurements of the perpendicular remanent magnetization $M_{\text{Z,R}}$.

In order to rationalize these findings, extensive first principles DFT calculations including the SOI self-consistently have been performed for (1×1) -Gr/ Co_n /HM₁₂ slabs with up to $n = 20$ Co layers. Such unusually thick slabs were found necessary to properly characterize the transition from thin Co films to the bulk *fcc* limit at around a Co thickness threshold value of 8 ML, where interface effects and finite size quantum oscillations start to become negligible. Beyond this threshold,

the Co film approaches the bulk Co *fcc* limit and shows an increasing in-plane anisotropy as the film grows thicker. Hence, we find that in the ideal *fcc* system the PMA, that is, positive MAE values, would vanish at much lower Co thicknesses than those experimentally observed. However, we have proved that the inclusion of structural defects in the form of twin boundaries to mimic a local *hcp* stacking in the Co film, actually seen in real samples mainly as stacking faults, can significantly delay the MAE switching and explain the observed critical thicknesses. Therefore, we reach the counterintuitive conclusion that it is precisely the existence of structural defects what prevents PMA degradation in these, otherwise almost perfect, heterostructures. In other words, the effect of the local structural defects on the macroscopic magnetization is to enhance the critical thickness at which it switches from out-of-plane to in-plane. Upon understanding of the PMA mechanism in these heterostructures, applications in the field of spin-orbitronics are foreseen. In particular, as stacking defects have a tendency to develop near the steps at the interfaces, the use of vicinal surfaces during growth might be a route to control the Co layer structure and consequently the magnetic anisotropy.

A sum rule analysis of the XMCD spectra shows a sizable orbital magnetic moment anisotropy Δm_L of the Co atoms that switches from out-of-plane to in-plane at similar Co thicknesses as $M_{Z,R}$ is observed to vanish in MOKE. DFT predicts a perpendicular OMMA, regardless of the presence or absence of stacking defects in the Co film, which shows an attenuation with increasing Co thickness compatible with the observations. Importantly, the calculations also reveal that this behavior is dominated by the large OMMA at the Gr/Co interface, and which is absent at the vacuum/Co interface.

4. METHODS

4.1. Experiments. Sample Preparation. The Gr-based epitaxial heterostructures were grown in ultrahigh-vacuum (UHV) condition on commercially available $\text{SrTiO}_3(111)$ - and $\text{Al}_2\text{O}_3(0001)$ -oriented oxide single crystals. The oxide crystals were ex/situ annealed in air at 1370 K for 2 h in order to obtain flat surfaces with large terraces prior to their insertion in the UHV chamber. Epitaxial (111)-oriented Pt and Ir buffers with thicknesses ranging from 10 to 30 nm were deposited by DC sputtering in 8×10^3 mbar Ar partial pressure at 670 K with a deposition rate of 0.3 Å/s. The quality of the fabricated Pt and Ir templates resembles the one of a single crystal, as demonstrated by LEED and XPS surface analyses.

The Gr monolayer was generated on Pt (Ir)/MgO(111) templates by exposing the samples kept at 1025 K in UHV (1×10^9 mbar) to ethylene gas at a partial pressure of 2×10^8 mbar for 30 min. The Gr/Pt/oxide(111) sample was cooled down to RT and Co was deposited on the top by e-beam evaporation at RT with a deposition rate of 0.04 Å/s. The sample was gradually heated up to 550 K while acquiring XPS spectra to verify in real time the intercalation of Co underneath the Gr sheet. The XPS spectrum of Co is not modified by the presence of Co–C,²⁰ which rules out diffusion of C. Once the intercalation was completed, the resulting sample was Gr/Co/Pt/oxide(111).

High-Resolution STEM. Electron microscopy observations were carried out in a JEOL ARM200cF microscope equipped with a CEOS spherical aberration corrector and a Gatan Quantum EEL spectrometer at the Centro Nacional de Microscopía Electrónica (CNME) at the University Complutense of Madrid. Specimens were prepared by conventional methods, including mechanical polishing and Ar ion milling.

Polar Kerr Magnetometry and Microscopy. The RT vectorial-Kerr experiments were performed in polar configuration by using p-polarized light (with 632 nm wavelength) focused on the sample

surface and analyzing the two orthogonal components of the reflected light. This provides the simultaneous determination of the hysteresis loops of the out-of-plane and in-plane magnetization components, that is, M_z and M_x , by sweeping the magnetic field along the sample out-of-plane (\hat{z}) direction.

XAS-XMCD. The XAS and magnetic circular dichroism experiments were carried out at the BOREAS beamline of the ALBA synchrotron using the fully circularly polarized X-ray beam produced by an APPLE-II type undulator.⁵⁵ The base pressure during measurements was $\sim 1 \times 10^{-10}$ mbar. The X-ray beam was focused to about $500 \times 500 \mu\text{m}^2$, and a gold mesh has been used for incident flux signal normalization. The XAS signal was measured with a Keithley 428 current amplifier via the sample-to-ground drain current (total electron yield TEY signal). The magnetic field was generated collinearly with the incoming X-ray direction by a superconducting vector cryomagnet (Scientific Magnetics). To obtain the spin averaged XAS and the XMCD, the absorption spectra were measured as a function of the photon energy both for parallel and antiparallel orientation ($\mu^+(E)$ and $\mu^-(E)$) of the photon spin and the magnetization of the sample. We recall that such XMCD measurements at the Co and $L_{2,3}$ absorption edges provide direct element-specific information on the magnitude and sign of the projection of Co magnetizations along the beam (and field) direction.

4.2. Calculations. DFT calculations have been carried out with the GREEN code^{56,57} and its interface to the SIESTA DFT-pseudopotential package⁵⁸ using the PBE exchange and correlation functional⁵⁹ and the fully relativistic pseudopotential (FR-PP) approach⁶⁰ to include the SOI self-consistently. The basis set consisted of strictly localized atomic orbitals generated following a double- ζ scheme for all atoms and employing a confinement energy (energy cut-off) of 100 meV. Pseudocore corrections were included for the metal atoms in order to describe accurately magnetic and SOI-derived properties.⁶¹ The directions of the magnetic moments were not constrained, and they lead to a collinear arrangement both for Pt and Ir atoms (i.e., the tilting angles were always negligible). An electronic temperature $kT = 20$ meV was used for the Fermi–Dirac distribution function and ultra fine k -space grids of at least 75×75 relative to the (1×1) -HM lattice together with real space meshes with a resolution $\sim 0.04 \text{ \AA}^3$ (equivalent to mesh cut-offs between 1000 and 2000 Ry) were employed to ensure a proper convergence in all reported MAEs.

Although the results presented in the main text correspond to (1×1) -Gr/Co_{*n*}/HM₁₂ model structures consisting of a 12 layers thick *fcc* HM buffer layer (111) oriented with a varying number of Co layers following the *fcc* stacking sequence on top, $n = 1$ –20, plus a capping (1×1) -Gr layer (see Figure 3(A)), we additionally considered alternative models including structural defects such as TBs, varying the buffer layer thickness or considering different moiré patterns at the Gr/Co interface (a detailed description of all of them together with their most relevant structural parameters after the atomic relaxations, as well as tetragonally distorted Co *fcc* bulk phases, are provided in SI Section 4).

The magnetic anisotropy energy (MAE) is defined here as

$$\text{MAE} = E_{\text{tot}}^x - E_{\text{tot}}^z \quad (1)$$

where $E_{\text{tot}}^{x/z}$ stand for the total energies, including SOI terms fully self-consistently, for spins aligned along the OX and OZ axes, so that PMA corresponds to a positive value of the MAE.

The MAE is a property in the meV and sub-meV range, extremely sensitive to calculation parameters, particularly the basis size. In order to obtain accurate MAE values, the convergence of this quantity with calculation parameters (energy cutoff, reciprocal space sampling, smearing of the Fermi level) has been carefully checked. Furthermore, we have examined if the force theorem approach^{62–64} to obtain MAE values is a reliable method for the present systems. These tests are gathered in SI Section 7. With the aforementioned computational parameters, the self-consistent MAEs and those computed in the force theorem approximation are converged below 0.03 and 0.05 meV, respectively. The magnetic moments are converged below 0.01 μ_B .

In order to cross-check the accuracy of the SOI-derived properties calculated under the FR-PP approximation used in the SIESTA-GREEN code, we have performed selected benchmark calculations using the DFT full-potential linearized augmented planewaves (FLAPW) formalism,^{65,66} as implemented in the FLEUR code.⁶⁷ Same as for SIESTA-GREEN, we used the PBE exchange and correlation functional⁵⁹ while the SOI was included fully self-consistently.⁶³ The FLAPW basis set is constructed with sufficiently fine Monkhorst–Pack-point meshes⁶⁸ to sample the first Brillouin zone and used plane wave expansion cut-offs of 4 a.u. for the wave functions, and 12 a.u. for the density and potential. For the local basis, the Co 4s, 3p, 3d electrons were treated as valence states and the 3s as a local orbital. The partial wave expansions were constructed with a $l_{\text{max}} = 8$ cutoff in a muffin-tin sphere of radius of 1.2 Å. The Fermi energy was determined by smearing with a Fermi–Dirac function of $kT = 14$ meV. In particular, the FLEUR code was employed for the calculation of the MAEs and orbital magnetic momenta values of a strained free-standing Co monolayer and the bulk *fcc* and strained *hcp* Co limits. The comparison versus the SIESTA-GREEN values, shown in SI Tables S3, S4, provides an excellent agreement for the OMMs in all cases in spite of the use of a different basis, as well as for the MAEs in the bulk phases. A discrepancy of 0.7 meV is however found for the MAE of the free-standing monolayer.

■ ASSOCIATED CONTENT

Supporting Information

The Supporting Information is available free of charge at <https://pubs.acs.org/doi/10.1021/acsnm.0c03364>.

Additional experimental and theoretical data (PDF)

■ AUTHOR INFORMATION

Corresponding Authors

María Blanco-Rey – Departamento de Polímeros y Materiales Avanzados: Física, Química y Tecnología, Facultad de Química, Universidad del País Vasco UPV/EHU, 20080 Donostia-San Sebastián, Spain; Donostia International Physics Center, 20018 Donostia-San Sebastián, Spain; orcid.org/0000-0002-5189-6690; Email: maria.blanco@ehu.es

Paolo Perna – IMDEA Nanociencia, 28049 Madrid, Spain; orcid.org/0000-0001-8537-4834; Email: paolo.perna@imdea.org

Authors

Adrian Gudín – IMDEA Nanociencia, 28049 Madrid, Spain

Jose Manuel Díez – IMDEA Nanociencia, 28049 Madrid, Spain; Departamento de Física de la Materia Condensada, Instituto Nicolás Cabrera, and Condensed Matter Physics Center (IFIMAC), Universidad Autónoma de Madrid, 28049 Madrid, Spain

Alberto Anadón – IMDEA Nanociencia, 28049 Madrid, Spain

Pablo Olleros-Rodríguez – IMDEA Nanociencia, 28049 Madrid, Spain

Leticia de Melo Costa – IMDEA Nanociencia, 28049 Madrid, Spain; ALBA Synchrotron Light Source, 08290 Barcelona, Spain

Manuel Valvidares – ALBA Synchrotron Light Source, 08290 Barcelona, Spain; orcid.org/0000-0003-4895-8114

Pierluigi Gargiani – ALBA Synchrotron Light Source, 08290 Barcelona, Spain; orcid.org/0000-0002-6649-0538

Alejandra Guedeja-Marrón – IMDEA Nanociencia, 28049 Madrid, Spain; Departamento de Física de Materiales and Instituto Pluridisciplinar, Universidad Complutense de Madrid, 28040 Madrid, Spain

Mariona Cabero – Departamento de Física de Materiales and Instituto Pluridisciplinar, Universidad Complutense de Madrid, 28040 Madrid, Spain

María Varela – Departamento de Física de Materiales and Instituto Pluridisciplinar, Universidad Complutense de Madrid, 28040 Madrid, Spain

Carlos García-Fernández – Centro de Física de Materiales, 20018 Donostia-San Sebastián, Spain; Donostia International Physics Center, 20018 Donostia-San Sebastián, Spain

Mikhail M. Otrokov – IKERBASQUE, Basque Foundation for Science, 48013 Bilbao, Spain; Centro de Física de Materiales, 20018 Donostia-San Sebastián, Spain; Donostia International Physics Center, 20018 Donostia-San Sebastián, Spain

Julio Camarero – IMDEA Nanociencia, 28049 Madrid, Spain; Departamento de Física de la Materia Condensada, Instituto Nicolás Cabrera, and Condensed Matter Physics Center (IFIMAC), Universidad Autónoma de Madrid, 28049 Madrid, Spain

Rodolfo Miranda – IMDEA Nanociencia, 28049 Madrid, Spain; Departamento de Física de la Materia Condensada, Instituto Nicolás Cabrera, and Condensed Matter Physics Center (IFIMAC), Universidad Autónoma de Madrid, 28049 Madrid, Spain

Andrés Arnau – Departamento de Polímeros y Materiales Avanzados: Física, Química y Tecnología, Facultad de Química, Universidad del País Vasco UPV/EHU, 20080 Donostia-San Sebastián, Spain; Centro de Física de Materiales, 20018 Donostia-San Sebastián, Spain; Donostia International Physics Center, 20018 Donostia-San Sebastián, Spain; orcid.org/0000-0001-5281-3212

Jorge I. Cerdá – Instituto de Ciencia de Materiales de Madrid, 28049 Madrid, Spain

Complete contact information is available at:

<https://pubs.acs.org/doi/10.1021/acsnm.0c03364>

Notes

The authors declare no competing financial interest.

■ ACKNOWLEDGMENTS

Discussions with J.J. Saenz (Mole) and Raffaele Resta are kindly acknowledged. Financial support from MINECO (Grant Nos. RTI2018-097895-B-C41, RTI2018-097895-B-C42 and RTI2018-097895-B-C43 (FUN-SOC), PID2019-103910GB-I00, FIS2016-78591-C3-1-R and FIS2016-78591-C3-2-R (SKYTRON), PGC2018-098613-B-C21 (SpOrQMat), PCI2019-111908-2 and PCI2019-111867-2 (FLAGERA 3 grant SOgraphMEM)], from Regional Government of Madrid (grant number P2018/NMT-4321 (NANOMAG-COST-CM)) and from Gobierno Vasco-UPV/EHU (grant numbers GIU18/138 and IT-1246-19). We acknowledge experiments at ALBA BL29 via proposal no. 2019023333. IMDEA-Nanociencia acknowledges support from the “Severo Ochoa” Program for Centres of Excellence in R&D (MINECO, Grant SEV-2016-0686). Computational resources were partially provided by the DIPC computing center.

■ ADDITIONAL NOTE

¹In an approximation that takes into account only the atomic orbital spatial distribution, as it is the case of the present calculations (atomic OMM values are obtained from

projections of the Kohn–Sham wave functions on atomic orbitals), the $d_{x^2-y^2,xy}$ orbitals contribute to m_{Lz} while d_{z^2} and $d_{xz,yz}$ to m_{Lx} .²⁹ Since the latter in-plane contributions (corresponding to negative OMMA values) are attenuated in a bulk-like environment due to hybridization between atomic planes, the net result is a positive OMMA (see SI Section 10).

REFERENCES

- (1) Dieny, B.; Chshiev, M. Perpendicular magnetic anisotropy at transition metal/oxide interfaces and applications. *Rev. Mod. Phys.* **2017**, *89*, 025008.
- (2) Garcia, P. F. Perpendicular magnetic anisotropy in Pd/Co and Pt/Co thin-film layered structures. *J. Appl. Phys.* **1988**, *63*, S066–S073.
- (3) Su, C.-H.; Lo, S.-C.; van Lierop, J.; Lin, K.-W.; Ouyang, H. The intermixing induced perpendicular magnetic anisotropy in ultrathin Co/Pt multilayers. *J. Appl. Phys.* **2009**, *105*, 07C316.
- (4) Winkler, G.; Kobs, A.; Chuvilin, A.; Lott, D.; Schreyer, A.; Oepen, H. P. On the variation of magnetic anisotropy in Co/Pt(111) on silicon oxide. *J. Appl. Phys.* **2015**, *117*, 105306.
- (5) Yang, H.; Vu, A. D.; Hallal, A.; Rougemaille, N.; Coraux, J.; Chen, G.; Schmid, A. K.; Chshiev, M. Anatomy and giant enhancement of the perpendicular magnetic anisotropy of cobalt–graphene heterostructures. *Nano Lett.* **2016**, *16*, 145–151.
- (6) Rougemaille, N.; N'Diaye, A. T.; Coraux, J.; Vo-Van, C.; Fruchart, O.; Schmid, A. K. Perpendicular magnetic anisotropy of cobalt films intercalated under graphene. *Appl. Phys. Lett.* **2012**, *101*, 142403.
- (7) Zhao, S.; Zhou, Z.; Li, C.; Peng, B.; Hu, Z.; Liu, M. Low-Voltage Control of (Co/Pt) x Perpendicular Magnetic Anisotropy Heterostructure for Flexible Spintronics. *ACS Nano* **2018**, *12*, 7167–7173.
- (8) Xie, Q.; Lin, W.; Yang, B.; Shu, X.; Chen, S.; Liu, L.; Yu, X.; Breese, M. B. H.; Zhou, T.; Yang, M.; Zhang, Z.; Wang, S.; Yang, H.; Chai, J.; Han, X.; Chen, J. Giant Enhancements of Perpendicular Magnetic Anisotropy and Spin-Orbit Torque by a MoS₂ Layer. *Adv. Mater.* **2019**, *31*, 1900776.
- (9) Zhang, W.; Wong, P. K. J.; Zhou, X.; Rath, A.; Huang, Z.; Wang, H.; Morton, S. A.; Yuan, J.; Zhang, L.; Chua, R.; Zeng, S.; Liu, E.; Xu, F.; Ariando; Chua, D. H. C.; Feng, Y. P.; van der Laan, G.; Pennycook, S. J.; Zhai, Y.; Wee, A. T. S. Ferromagnet/Two-Dimensional Semiconducting Transition-Metal Dichalcogenide Interface with Perpendicular Magnetic Anisotropy. *ACS Nano* **2019**, *13*, 2253–2261.
- (10) Lin, W.; Yang, B.; Chen, A. P.; Wu, X.; Guo, R.; Chen, S.; Liu, L.; Xie, Q.; Shu, X.; Hui, Y.; Chow, G. M.; Feng, Y.; Carlotti, G.; Tacchi, S.; Yang, H.; Chen, J. Perpendicular Magnetic Anisotropy and Dzyaloshinskii–Moriya Interaction at an Oxide/Ferromagnetic Metal Interface. *Phys. Rev. Lett.* **2020**, *124*, 217202.
- (11) Soumyanarayanan, A.; Reyren, N.; Fert, A.; Panagopoulos, C. Emergent phenomena induced by spin–orbit coupling at surfaces and interfaces. *Nature* **2016**, *539*, 509–517.
- (12) Manchon, A.; Železný, J.; Miron, I. M.; Jungwirth, T.; Sinova, J.; Thiaville, A.; Garello, K.; Gambardella, P. Current-induced spin-orbit torques in ferromagnetic and antiferromagnetic systems. *Rev. Mod. Phys.* **2019**, *91*, 035004.
- (13) Manchon, A.; Pizzini, S.; Vogel, J.; Uhlir, V.; Lombard, L.; Ducruet, C.; Auffret, S.; Rodmacq, B.; Dieny, B.; Hochstrasser, M.; Panaccione, G. X-ray analysis of oxygen-induced perpendicular magnetic anisotropy in Pt/Co/AlO_x trilayers. *J. Magn. Magn. Mater.* **2008**, *320*, 1889–1892.
- (14) Nistor, C.; Balashov, T.; Kavich, J. J.; Lodi Rizzini, A.; Ballesteros, B.; Gaudin, G.; Auffret, S.; Rodmacq, B.; Dhesi, S.; Gambardella, P. Orbital moment anisotropy of Pt/Co/AlO_x heterostructures with strong Rashba interaction. *Phys. Rev. B* **2011**, *84*, 054464.
- (15) Ueno, T.; Sinha, J.; Inami, N.; Takeichi, Y.; Mitani, S.; Ono, K.; Hayashi, M. Enhanced orbital magnetic moments in magnetic heterostructures with interface perpendicular magnetic anisotropy. *Sci. Rep.* **2015**, *5*, 14858.
- (16) Ascolani, H.; Cerda, J.; de Andres, P.; de Miguel, J.; Miranda, R.; Heinz, K. Detecting stacking faults during epitaxial growth by low energy electron diffraction. *Surf. Sci.* **1996**, *345*, 320–330.
- (17) Vázquez de Parga, A. L.; García-Vidal, F. J.; Miranda, R. Detecting Electronic States at Stacking Faults in Magnetic Thin Films by Tunneling Spectroscopy. *Phys. Rev. Lett.* **2000**, *85*, 4365–4368.
- (18) Doi, K.; Minamitani, E.; Yamamoto, S.; Arafune, R.; Yoshida, Y.; Watanabe, S.; Hasegawa, Y. Electronic and magnetic effects of a stacking fault in cobalt nanoscale islands on the Ag(111) surface. *Phys. Rev. B* **2015**, *92*, 064421.
- (19) Ajejas, F.; Gudín, A.; Guerrero, R.; Anadón Barcelona, A.; Diez, J. M.; de Melo Costa, L.; Olleros, P.; Niño, M. A.; Pizzini, S.; Vogel, J.; Valvidares, M.; Gargiani, P.; Cabero, M.; Varela, M.; Camarero, J.; Miranda, R.; Perna, P. Unraveling Dzyaloshinskii–Moriya Interaction and Chiral Nature of Graphene/Cobalt Interface. *Nano Lett.* **2018**, *18*, 5364–5372.
- (20) Ajejas, F.; Anadon, A.; Gudín, A.; Diez, J. M.; Ayani, C. G.; Olleros-Rodríguez, P.; de Melo Costa, L.; Navío, C.; Gutiérrez, A.; Calleja, F.; Vázquez de Parga, A. L.; Miranda, R.; Camarero, J.; Perna, P. Thermally Activated Processes for Ferromagnet Intercalation in Graphene-Heavy Metal Interfaces. *ACS Appl. Mater. Interfaces* **2020**, *12*, 4088–4096.
- (21) Rougemaille, N.; N'Diaye, A. T.; Coraux, J.; Vo-Van, C.; Fruchart, O.; Schmid, A. K. Perpendicular magnetic anisotropy of cobalt films intercalated under graphene. *Appl. Phys. Lett.* **2012**, *101*, 142403.
- (22) Decker, R.; Brede, J.; Atodiresei, N.; Caciuc, V.; Blügel, S.; Wiesendanger, R. Atomic-scale magnetism of cobalt-intercalated graphene. *Phys. Rev. B* **2013**, *87*, 041403.
- (23) Gargiani, P.; Cuadrado, R.; Vasili, H. B.; Pruneda, M.; Valvidares, M. Graphene-based synthetic antiferromagnets and ferrimagnets. *Nat. Commun.* **2017**, *8*, 699.
- (24) Vlaic, S.; Rougemaille, N.; Artaud, A.; Renard, V.; Huder, L.; Rouvière, J.-L.; Kimouche, A.; Santos, B.; Locatelli, A.; Guisset, V.; David, P.; Chapelier, C.; Magaud, L.; Canals, B.; Coraux, J. Graphene as a Mechanically Active, Deformable Two-Dimensional Surfactant. *J. Phys. Chem. Lett.* **2018**, *9*, 2523–2531.
- (25) Sutter, P.; Sadowski, J. T.; Sutter, E. Graphene on Pt(111): Growth and substrate interaction. *Phys. Rev. B* **2009**, *80*, 245411.
- (26) N'Diaye, A. T.; Coraux, J.; Plasa, T. N.; Busse, C.; Michely, T. Structure of epitaxial graphene on Ir(111). *New J. Phys.* **2008**, *10*, 043033.
- (27) Cerda, J. R.; de Andres, P. L.; Cebollada, A.; Miranda, R.; Navas, E.; Schuster, P.; Schneider, C. M.; Kirschner, J. Epitaxial growth of cobalt films on Cu(100): a crystallographic LEED determination. *J. Phys.: Condens. Matter* **1993**, *5*, 2055–2062.
- (28) Thole, B. T.; Carra, P.; Sette, F.; van der Laan, G. X-ray circular dichroism as a probe of orbital magnetization. *Phys. Rev. Lett.* **1992**, *68*, 1943–1946.
- (29) Stöhr, J. Exploring the microscopic origin of magnetic anisotropies with X-ray magnetic circular dichroism (XMCD) spectroscopy. *J. Magn. Magn. Mater.* **1999**, *200*, 470–497.
- (30) Chen, C. T.; Idzerda, Y. U.; Lin, H.-J.; Smith, N. V.; Meigs, G.; Chaban, E.; Ho, G. H.; Pellegrin, E.; Sette, F. Experimental Confirmation of the X-Ray Magnetic Circular Dichroism Sum Rules for Iron and Cobalt. *Phys. Rev. Lett.* **1995**, *75*, 152–155.
- (31) Chappert, C.; Bruno, P. Magnetic anisotropy in metallic ultrathin films and related experiments on cobalt films (invited). *J. Appl. Phys.* **1988**, *64*, S736–S741.
- (32) Bruno, P. Tight-binding approach to the orbital magnetic moment and magnetocrystalline anisotropy of transition-metal monolayers. *Phys. Rev. B* **1989**, *39*, 865–868.
- (33) Błoński, P.; Lehnert, A.; Dennler, S.; Rusponi, S.; Etzkorn, M.; Moulas, G.; Bencok, P.; Gambardella, P.; Brune, H.; Hafner, J. Magnetocrystalline anisotropy energy of Co and Fe adatoms on the (111) surfaces of Pd and Rh. *Phys. Rev. B* **2010**, *81*, 104426.

- (34) Yang, H.; Vu, A. D.; Hallal, A.; Rougemaille, N.; Coraux, J.; Chen, G.; Schmid, A. K.; Chshiev, M. Anatomy and Giant Enhancement of the Perpendicular Magnetic Anisotropy of Cobalt–Graphene Heterostructures. *Nano Lett.* **2016**, *16*, 145–151.
- (35) Steiner, S.; Khmelevskiy, S.; Marsmann, M.; Kresse, G. Calculation of the magnetic anisotropy with projected-augmented-wave methodology and the case study of disordered Fe_{1-x}Co_x alloys. *Phys. Rev. B* **2016**, *93*, 224425.
- (36) Wolloch, M.; Suess, D.; Mohn, P. Influence of antisite defects and stacking faults on the magnetocrystalline anisotropy of FePt. *Phys. Rev. B* **2017**, *96*, 104408.
- (37) Cabral, L.; Aragón, F. H.; Villegas-Lelovsky, L.; Lima, M. P.; Macedo, W. A. A.; Da Silva, J. L. F. Tuning the Magnetic Properties of FeCo Thin Films through the Magnetoelastic Effect Induced by the Au Underlayer Thickness. *ACS Appl. Mater. Interfaces* **2019**, *11*, 1529–1537.
- (38) Rodmacq, B.; Manchon, A.; Ducruet, C.; Auffret, S.; Dieny, B. Influence of thermal annealing on the perpendicular magnetic anisotropy of Pt/Co/AlOx trilayers. *Phys. Rev. B* **2009**, *79*, 024423.
- (39) Olleros-Rodríguez, P.; Guerrero, R.; Camarero, J.; Chubykalo-Fesenko, O.; Perna, P. Intrinsic mixed Bloch–Néel character and chirality switch of skyrmions in asymmetric epitaxial trilayer. *ACS Appl. Mater. Interfaces* **2020**, *12*, 25419–25427.
- (40) Ferrer, S.; Alvarez, J.; Torrelles, X.; Lundgren, E.; Fajardo, P. Measurement of the magnetism of a single atomic plane with X-ray diffraction. *Phys. B* **1998**, *248*, 9–13.
- (41) Belabbes, A.; Bihlmayer, G.; Bechstedt, F.; Blügel, S.; Manchon, A. Hund's Rule-Driven Dzyaloshinskii–Moriya Interaction at 3d–5d Interfaces. *Phys. Rev. Lett.* **2016**, *117*, 247202.
- (42) Keshavarz, S.; Kvashnin, Y. O.; Di Marco, I.; Delin, A.; Katsnelson, M. I.; Lichtenstein, A. I.; Eriksson, O. Layer-resolved magnetic exchange interactions of surfaces of late 3d elements: Effects of electronic correlations. *Phys. Rev. B* **2015**, *92*, 165129.
- (43) Baumann, S.; Donati, F.; Stepanow, S.; Rusponi, S.; Paul, W.; Gangopadhyay, S.; Rau, I. G.; Pacchioni, G. E.; Gragnaniello, L.; Pivetta, M.; Dreiser, J.; Piamonteze, C.; Lutz, C. P.; Macfarlane, R. M.; Jones, B. A.; Gambardella, P.; Heinrich, A. J.; Brune, H. Origin of Perpendicular Magnetic Anisotropy and Large Orbital Moment in Fe Atoms on MgO. *Phys. Rev. Lett.* **2015**, *115*, 237202.
- (44) Gallardo, I.; Arnau, A.; Delgado, F.; Baltic, R.; Singha, A.; Donati, F.; Wäckerlin, C.; Dreiser, J.; Rusponi, S.; Brune, H. Large effect of metal substrate on magnetic anisotropy of Co on hexagonal boron nitride. *New J. Phys.* **2019**, *21*, 073053.
- (45) Lehnert, A.; Dennler, S.; Błoński, P.; Rusponi, S.; Etzkorn, M.; Moulas, G.; Bencok, P.; Gambardella, P.; Brune, H.; Hafner, J. Magnetic anisotropy of Fe and Co ultrathin films deposited on Rh(111) and Pt(111) substrates: An experimental and first-principles investigation. *Phys. Rev. B* **2010**, *82*, 094409.
- (46) van der Laan, G. Line shape of 2p magnetic-x-ray-dichroism spectra in 3d metallic systems. *Phys. Rev. B* **1997**, *55*, 8086–8089.
- (47) Gambardella, P.; Rusponi, S.; Veronese, M.; Dhessi, S. S.; Grazioli, C.; Dallmeyer, A.; Cabria, I.; Zeller, R.; Dederichs, P. H.; Kern, K.; Carbone, C.; Brune, H. Giant Magnetic Anisotropy of Single Cobalt Atoms and Nanoparticles. *Science* **2003**, *300*, 1130–1133.
- (48) Blanco-Rey, M.; Cerdá, J. I.; Arnau, A. Validity of perturbative methods to treat the spin–orbit interaction: application to magnetocrystalline anisotropy. *New J. Phys.* **2019**, *21*, 073054.
- (49) Andersson, C.; Sanyal, B.; Eriksson, O.; Nordström, L.; Karis, O.; Arvanitis, D.; Konishi, T.; Holub-Krappe, E.; Dunn, J. H. Influence of Ligand States on the Relationship between Orbital Moment and Magnetocrystalline Anisotropy. *Phys. Rev. Lett.* **2007**, *99*, 177207.
- (50) van der Laan, G. Microscopic origin of magnetocrystalline anisotropy in transition metal thin films. *J. Phys.: Condens. Matter* **1998**, *10*, 3239–3253.
- (51) Thole, B. T.; Carra, P.; Sette, F.; van der Laan, G. X-ray circular dichroism as a probe of orbital magnetization. *Phys. Rev. Lett.* **1992**, *68*, 1943–1946.
- (52) Kuneš, J.; Oppeneer, P. M. Exact many-body sum rule for the magneto-optical spectrum of solids. *Phys. Rev. B* **2000**, *61*, 15774–15777.
- (53) Souza, I.; Vanderbilt, D. Dichroic *f*-sum rule and the orbital magnetization of crystals. *Phys. Rev. B* **2008**, *77*, 054438.
- (54) Resta, R. Magnetic circular dichroism versus orbital magnetization. *Phys. Rev. Research* **2020**, *2*, 023139.
- (55) Barla, A.; Nicolás, J.; Cocco, D.; Valvidares, S. M.; Herrero-Martín, J.; Gargiani, P.; Moldes, J.; Ruget, C.; Pellegrin, E.; Ferrer, S. Design and performance of BOREAS, the beamline for resonant X-ray absorption and scattering experiments at the ALBA synchrotron light source. *J. Synchrotron Radiat.* **2016**, *23*, 1507–1517.
- (56) Cerdá, J.; Van Hove, M. A.; Sautet, P.; Salmeron, M. Efficient method for the simulation of STM images. I. Generalized Green-function formalism. *Phys. Rev. B* **1997**, *56*, 15885–15899.
- (57) Rossen, E. T. R.; Flipse, C. F. J.; Cerdá, J. I. Lowest order in inelastic tunneling approximation: Efficient scheme for simulation of inelastic electron tunneling data. *Phys. Rev. B* **2013**, *87*, 235412.
- (58) Soler, J. M.; Artacho, E.; Gale, J. D.; García, A.; Junquera, J.; Ordejón, P.; Sánchez-Portal, D. The SIESTA method for ab initio order-*N* materials simulation. *J. Phys.: Condens. Matter* **2002**, *14*, 2745.
- (59) Perdew, J. P.; Burke, K.; Ernzerhof, M. Generalized Gradient Approximation Made Simple [Phys. Rev. Lett. **77**, 3865 (1996)]. *Phys. Rev. Lett.* **1997**, *78*, 1396.
- (60) Cuadrado, R.; Cerdá, J. I. Fully relativistic pseudopotential formalism under an atomic orbital basis: spin-orbit splittings and magnetic anisotropies. *J. Phys.: Condens. Matter* **2012**, *24*, 086005.
- (61) Blöchl, P. E. Projector augmented-wave method. *Phys. Rev. B* **1994**, *50*, 17953.
- (62) Weinert, M.; Watson, R. E.; Davenport, J. W. Total-energy differences and eigenvalue sums. *Phys. Rev. B* **1985**, *32*, 2115–2119.
- (63) Li, C.; Freeman, A. J.; Jansen, H. J. F.; Fu, C. L. Magnetic anisotropy in low-dimensional ferromagnetic systems: Fe monolayers on Ag(001), Au(001), and Pd(001) substrates. *Phys. Rev. B* **1990**, *42*, 5433–5442.
- (64) Daalderop, G. H. O.; Kelly, P. J.; Schuurmans, M. F. H. First-principles calculation of the magnetocrystalline anisotropy energy of iron, cobalt, and nickel. *Phys. Rev. B* **1990**, *41*, 11919–11937.
- (65) Krakauer, H.; Posternak, M.; Freeman, A. J. Linearized augmented plane-wave method for the electronic band structure of thin films. *Phys. Rev. B* **1979**, *19*, 1706–1719.
- (66) Wimmer, E.; Krakauer, H.; Weinert, M.; Freeman, A. J. Full-potential self-consistent linearized-augmented-plane-wave method for calculating the electronic structure of molecules and surfaces: O₂ molecule. *Phys. Rev. B* **1981**, *24*, 864–875.
- (67) FLEUR: <http://www.flapw.de>.
- (68) Monkhorst, H. J.; Pack, J. D. Special points for Brillouin-zone integrations. *Phys. Rev. B* **1976**, *13*, 5188.